

Flux tunable graphene-based superconducting quantum circuits coupled to 3D cavity

Kuei-Lin Chiu^{1,*}, Youyi Chang¹, Avishma J. Lasrado¹, Cheng-Han Lo¹, Yung-Hsiang Chen¹,
Tao-Yi Hsu¹, Yen-Chih Chen¹, Yi-Chen Tsai³, Samina², Yen-Hsiang Lin², Chung-Ting Ke^{3,*}

¹*Department of Physics, National Sun Yat-Sen University, Kaohsiung 80424, Taiwan*

²*Department of physics, National Tsing-Hua University, Hsinchu 300044, Taiwan and*

³*Institute of Physics, Academia Sinica, Taipei 115201, Taiwan*

(Dated: December 8, 2023)

Correlation between transmon and its composite Josephson junctions (JJ) plays an important role in designing new types of superconducting qubits based on quantum materials. It is desirable to have a type of device that not only allows exploration for use in quantum information processing but also probing intrinsic properties in the composite JJs. Here, we construct a flux-tunable 3D transmon-type superconducting quantum circuit made of graphene as a proof-of-concept prototype device. This 3D transmon-type device not only enables coupling to 3D cavities for microwave probes but also permits DC transport measurements on the same device, providing useful connections between transmon properties and critical currents associated with JJ's properties. We have demonstrated how flux-modulation in cavity frequency and DC critical current can be correlated under the influence of Fraunhofer pattern of JJs in an asymmetric SQUID. The correlation analysis was further extended to link the flux-modulated transmon properties, such as flux-tunability in qubit and cavity frequencies, with SQUID symmetry analysis based on DC measurements. Our study paves the way towards integrating novel materials for exploration of new types of quantum devices for future technology while probing underlying physics in the composite materials.

Keywords:

I. INTRODUCTION

Josephson junction (JJ) is a key component in superconducting qubits. Apart from the commonly used Al/Al₂O₃/Al S-I-S junctions (I stands for insulator and S stands for superconductor), there is a growing interest in using S-N-S junctions (N stands for normal metals, but can also be semiconductors) as core components in superconducting qubits [1–8]. Quantum materials, owing to their rich internal degrees of freedom unexplored, provide versatile functions to be integrated as a main ingredient in superconducting qubits [9–12]. Graphene and two-dimensional electron gas (2DEG), due to their 2D hence gate tunable natures, can serve as normal metals in S-N-S junctions, forming gate tunable transmons generally referred as gatemons [1–5]. Semiconducting InAs nanowires can be similarly regarded and have been demonstrated as gatemons [6–8] or resonator-type superconducting devices [13, 14]. On the other hand, 2D materials such as NbSe₂ have been used as superconductors in S-N-S junctions while hBN and MoS₂ have been used as barrier layers in S-I-S junctions for transmon-type of devices [15–17]. Furthermore, using topological materials as the weak link in JJs may provide a different route to realizing the exotic Majorana bound states where 4π -period phase modulation is expected [18]. Therefore, with transmon architectures, one will be able to probe the

topological nature of the composite topological Josephson junctions [19–21].

Transport measurements often provide fundamental information in probing JJ's internal degrees of freedom, including conventional Andreev bound states (ABSs) and exotic Majorana modes, which are distinguished by 2π vs 4π periodic contributions to the supercurrent [22]. However, due to its slow probing speed, it cannot access to dynamical probing and often suffers from quasiparticle poisoning, which tends to restore 4π periodic supercurrent to 2π periodicity in topological junctions [22, 23]. On the other hand, microwave technique used in superconducting qubits is a powerful tool that usually operates in the time scale of microseconds [24], fast enough to probe dynamic processes such as quasiparticle tunneling that often happens in the time scale between μ s and ms [23, 25, 26]. Therefore, it is desirable to have a type of device that can not only allow transport measurement to reveal critical current information associated with ABSs, but also permits transmon-type microwave measurements for potential probing the dynamic properties of ABSs.

In this letter, we construct 3D transmon-type superconducting quantum circuits made of graphene as a proof-of-concept prototype device to address the aforementioned desires. This graphene-based superconducting quantum circuit consists of a pair of capacitor pads, which serve as the antenna to interact with microwave in a 3D copper cavity as well as for the bond pads in DC transport measurements. From both type of measurements, we find correlation between two approaches, which lay the foundations enabling exploration of new material-based quantum devices for future technology

* Corresponding author: K. L. Chiu (klc@mail.nsysu.edu.tw)

* Corresponding author: C. T. Ke (ctke@gate.sinica.edu.tw)

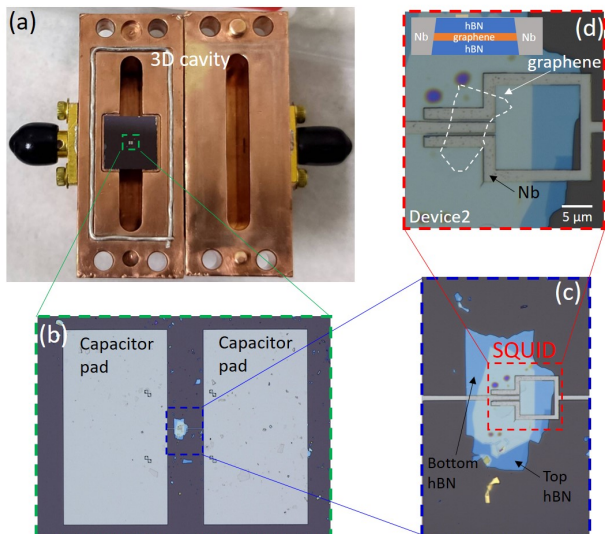


FIG. 1: Optical micrograph of a flux tunable graphene-based superconducting quantum circuit coupled to a 3D copper cavity. This device is referred as device 2 in this manuscript. (a) 3D copper cavity with a device residing in the center. (b) Optical micrograph of the device, consisting of the shunting capacitor with SQUID loop in the center. (c) Optical micrograph showing the SQUID made of graphene and superconductor Nb. The graphene flake was sandwiched between two hBN layers [inset in (d)] before making edge contacts of Nb. (d) The zoom-in image of (c) showing the geometry of the SQUID, which is formed by a square loop (line width: $2 \mu\text{m}$; inner area: $16 \mu\text{m} \times 16 \mu\text{m}$) with encapsulated graphene linking two 500 nm gaps. The inset shows the hBN/graphene/hBN sandwich structure with edge contacts.

while probing underlying physics in the composite materials.

II. DEVICE FABRICATION AND MEASUREMENT SETUP

Fig. 1 shows the optical micrograph of our flux tunable graphene-based superconducting quantum circuits coupled to a 3D copper cavity. This transmon-type quantum circuit consists of a superconducting quantum interference device (SQUID) made of two Nb-Graphene-Nb junctions, with an enclosed loop of Nb at a nominal size of $16 \times 16 \mu\text{m}^2$ [Fig. 1 (d)]. In order to preserve the graphene quality, the exfoliated graphene is encapsulated by hexagonal Boron Nitride (hBN) [Fig. 1 (c)], and the SQUID is fabricated based on the edge contact techniques [27], as described in section I in Supplementary Materials (SM). The SQUID is shunted by a capacitor formed between two rectangular capacitor pads as shown in Fig. 1 (b), which effectively forms a transmon. In qubit type of microwave measurements, these two capacitor pads act as an antenna to interact with electromagnetic field in 3D cavities; while in DC transport measurements, these two

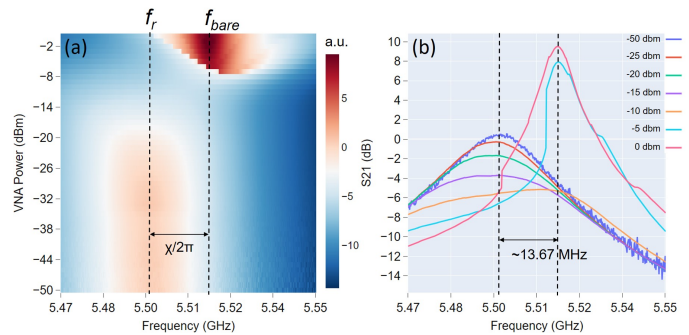


FIG. 2: (a) Qubit punch-out measurement of device 1 [Fig. S2 (c)], confirming the presence of graphene JJs by showing a dispersive shift $\chi/2\pi$. (b) Linecuts in (a) at different powers. The spectrum peaks at around 5.5 GHz at low power, then undergoes a broad regime at $P \approx -15 \text{ dBm}$, and finally enters a bright regime at $P = 0 \text{ dBm}$, with a narrower line shape of Lorentzian and a dispersive shift of around 13.67 MHz .

capacitor pads are used as bond pads.

The measurement scheme for microwave and DC transport exploited in this work is illustrated in Fig. S3 (a) and (b), respectively. For microwave measurements, as shown in Fig. 1 (a), the devices were placed in a two-ports 3D copper cavity to provide good thermal conductivity and to allow externally applied magnetic fields to thread through the cavity for flux-tuning. Our 3D cavity is designed as a rectangular resonator, the resonance frequency of which is given by the formula: $f_{mnl} = \frac{c}{2\pi\sqrt{\mu_r\epsilon_r}} \sqrt{(\frac{m\pi}{a})^2 + (\frac{n\pi}{b})^2 + (\frac{l\pi}{d})^2}$, where a , b and d represent the three-dimensional lengths of the rectangular resonator while m , n and l represent the mode numbers. Generally, the transmon qubit placed in the center of the cavity chamber [Fig. 1 (a)] is primarily coupled with the electric field of TE_{101} mode [28]. In this work, three devices labeled as 1, 2 and 3 were characterized, and they were placed in a 5.5 GHz (device 1 and 2) cavity and a 6.03 GHz (device 3) cavity for microwave measurements, respectively. For calibrating 3D cavities, performing transmission (S_{21}) and DC transport measurements, please refer to section II in SM.

III. DEVICE CHARACTERIZATION AND RESULTS

We first performed the qubit punch-out measurements on device 1, in which the transmission of the two-ports 3D cavity was measured *via* S_{21} measurement of a vector network analyzer (VNA) as a function of readout power and frequency, as shown in Fig. 2(a). This is a conventional way to confirm the existence of JJ [29], where the resonant frequency of the cavity (f_r) shifts toward the qubit frequency at large enough power around 0 dBm . Fig. 2(b) shows the linecuts at different readout powers.

At lower powers from -50 dBm to -15 dBm, the cavity frequency centers around 5.5 GHz with an asymmetric line shape, indicating a canonical behavior of a Kerr-Duffing oscillator [30]. After undergoing a broad range (-15 dBm $\leq P \leq$ -8 dBm), the cavity response re-appears with a narrower line shape of Lorentzian and a frequency shifted to 5.516 GHz at $P = 0$ dBm, which is known as the bare cavity frequency (f_{bare}) at which the cavity would resonate in the absence of JJs. The dispersive shift $\chi/2\pi$ of around 13.67 MHz between cavity's frequency at low power (f_r) and at high-power (f_{bare}) allows us to estimate the qubit-cavity coupling strength g *via* $\chi = g^2/\Delta$ and $\Delta = 2\pi(f_r - f_q)$, where f_q is qubit frequency. To deduce f_q , we have performed two-tone measurements (data not shown), but no qubit transition was found in the probed frequency range of 4 to 12 GHz. Although we cannot obtain direct information about f_q *via* two-tone, we have relied on critical current in transport data to estimate both f_q and g , as discussed in section IV in SM.

Microwave measurements of flux-tuning on graphene SQUID was executed by measuring the resonant cavity frequency at a low readout power (-55 dBm) while tuning the DC source current passing through the home-made superconducting coil around the cooper 3D cavity. The flux-modulated resonant cavity frequency for device 1, 2 and 3 is shown in Fig. 3(a), (b) and (c), respectively. Interestingly, while a periodic modulation of cavity frequency was observed in device 2 and 3 [Fig. 3(b) and (c)], as being commonly seen in conventional Al/Al₂O₃-based transmons [31], there is an additional larger-period flux modulation observed in device 1, as indicated by the dashed box in Fig. 3(a). This larger-period modulation is superimposed on a fine modulation presumably from SQUID critical current oscillation, with a ratio of 10 to 1 in period. We attribute this additional modulation to the Fraunhofer oscillation resulted from the composing graphene JJs (section III in SM). In a symmetric SQUID whose interference pattern is modulated by the Fraunhofer diffraction patterns of each JJ, the total critical current can be described as [32]:

$$I_c(B) = 2I_c(0) \left| \sin\left(\frac{\pi\Phi_J}{\phi_0}\right) / \left(\frac{\pi\Phi_J}{\phi_0}\right) \right| \left| \cos\frac{\pi\Phi}{\phi_0} \right| \quad (1)$$

where $I_c(0)$ is the critical current of each junction at zero magnetic field, Φ_J is the flux threading through the single junction area, Φ is the flux threading through the loop area of SQUID and $\phi_0 = h/2e$ is the flux quanta. The first term in equation 1 represents the Fraunhofer pattern which consists of a central lobe and a series of sub-lobes, while the second term represents SQUID oscillations. The ratio between the SQUID loop area and JJ area determines how many SQUID oscillations reside in a lobe of Fraunhofer pattern. The central lobe in Fraunhofer pattern contains twice the number of SQUID oscillations in other sub-lobes. The modulation behavior of

equation 1 with respect to the applied flux is illustrated in Fig. 4(a), with the SQUID loop area set to be 10 times of the junction area, to emulate the situation observed in Fig. 3(a) [see detailed discussions in section III of SM]. As can be seen in Fig. 4(a), the Fraunhofer pattern indicated by the blue solid lines is modulating the SQUID critical current oscillations indicated by the red solid lines. We can relate the Fraunhofer effect-mediated SQUID critical current with different transmon's parameters. Since Josephson energy $E_J = \frac{\Phi_0 I_C}{2\pi}$ is proportional to I_C while qubit frequency $f_q \approx \sqrt{8E_J E_C}/h$ is proportional to $\sqrt{I_C}$, their flux modulation under Fraunhofer effect is shown in red and green solid lines in Fig. 4(a), respectively. By controlling the magnetic flux threading through the SQUID loop, we are able to modify the critical current, hence E_J and f_q , which leads to different dispersive shift $\chi = -g^2/2\pi(f_q - f_r)$ to be measured in cavity frequency. In Fig. 4(b), we show the schematically simulated dispersive shift under the influence of Fraunhofer effect (see discussions in section III of SM). Due to the effect of square root and reciprocal, the large variation in height of Fraunhofer lobes [blues curve in Fig. 4(a)] has become a relatively small variation in dispersive shift as shown in Fig. 4(b).

In order to gain more insight into how critical current is correlated with the microwave measurement of our graphene-based quantum circuits, we have performed DC transport measurements on device 1, 2 and 3, as shown in Fig. 3(d), (e) and (f), respectively. All devices have shown the SQUID modulations with Fraunhofer pattern, with 82 oscillations in the central lobe for device 1, 61 oscillations in that for device 2 and 55 oscillations in that for device 3 [bottom panels of Fig. 3(d), (e) and (f)]. Notably, for device 1, Fig. 3(d) indicates that the number of SQUID oscillations in the Fraunhofer sub-lobe is 41, which is four times of the number 10 observed in the microwave measurement shown in Fig. 3(a). One possible reason for the periods' ratio discrepancy between microwave and DC measurements is due to different cool down. While the sample moved from one setup to another, the junction degradation may lead to a change in the ratio between the Fraunhofer period and the SQUID period. However, in later analysis, we found that SQUID's JJs in device 1 are asymmetric with a ratio $I_{C1} : I_{C2} = 1:4$, which coincides with the above ratio 10:41 comparing microwave with DC results. Thus, we attribute the Fraunhofer modulation observed in microwave measurement to the larger junction in the asymmetric SQUID, with a area ratio to SQUID loop 1:10 as indicated by JJ₂ in Fig. S4(c) (see discussions in section III of SM).

The Fraunhofer pattern modulation was not pronounced in the microwave measurements of device 2 [Fig. 3(b)] and device 3 [Fig. 3(c)], while the transport data as shown in Fig. 3(e) and Fig. 3(f) present Fraunhofer modulation with the central lobes containing large number of

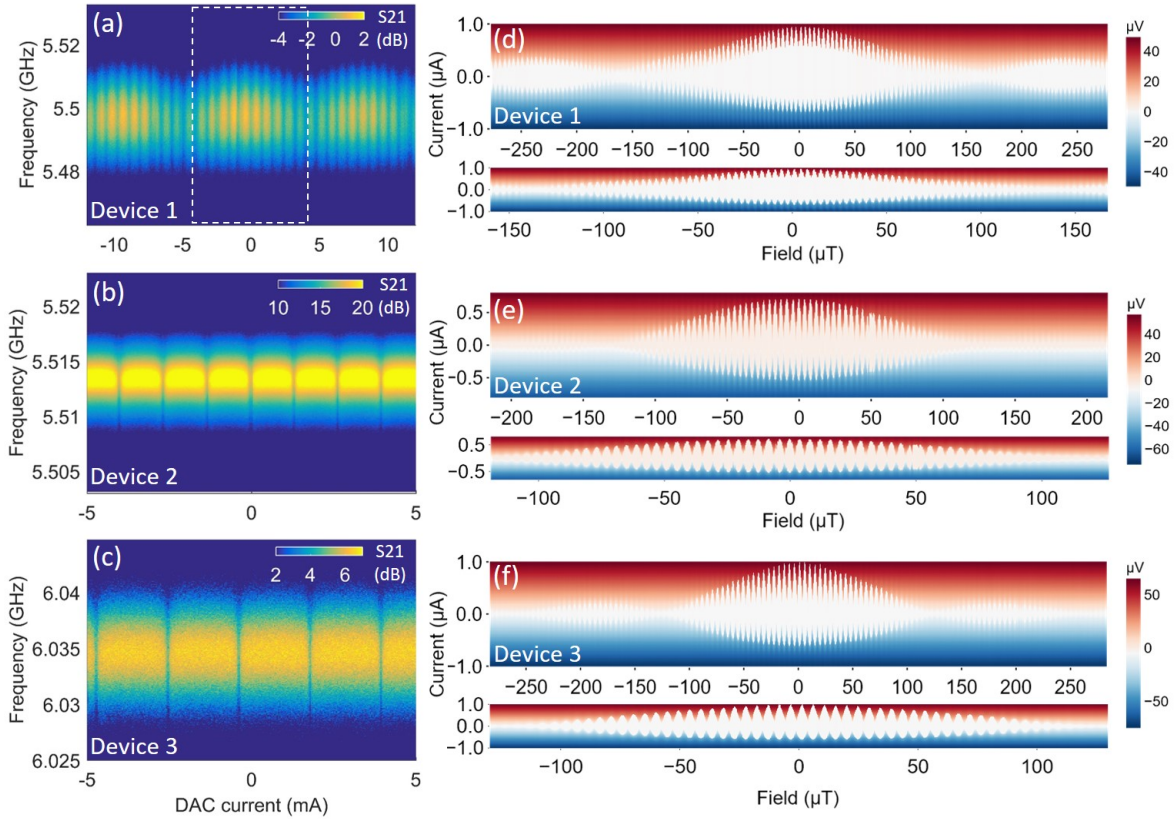


FIG. 3: Flux modulation of cavity frequency (microwave measurements) and critical current (DC transport measurements) of our graphene-based superconducting quantum circuits in different cool-down. (a) - (c) Flux modulation of cavity frequency for device 1, 2 and 3. The dashed rectangle in (a) indicates 10 SQUID oscillations in a Fraunhofer lobe. (d) - (f) Flux modulation of SQUID critical current for device 1, 2 and 3. The bottom panels show the SQUID oscillations in the Fraunhofer central lobe for each device.

SQUID oscillations (61 for device 2 and 55 for device 3). This can be understood as illustrated in Fig. S4 (a) and (b), where different ratio of area between junction to SQUID loop leads to 10 and 40 SQUID oscillations residing in a Fraunhofer sub-lobe, respectively. Thus, if we compare 10 SQUID oscillations in each case, the Fraunhofer modulation on SQUID oscillations is more pronounced in large SQUID loop-to-junction area ratio, as illustrated in Fig. 4(c) and (d), respectively (we used 40 SQUID oscillations as an example but the same concept apply to the case of device 2 and device 3). In addition, we note that the heights of the three Fraunhofer sub-lobes observed in Fig. 3(a) are similar (around 5.52 GHz). We speculate that these sub-lobes from JJ_2 do not reside in the strong-modulating central lobe of the smaller junction (JJ_1), but locate in JJ_1 's outer sub-lobe as shown in the inset of Fig. S4(c), possibly due to the remanent magnetic field in our superconducting coil. In a similar regard, the flux modulation shown in Fig. 3(b) and Fig. 3 (c) also origin from the outer Fraunhofer sub-lobes, which has less modulation on SQUID oscillations compared to that in the central lobe, as evident in the

transport data shown in Fig. 3(e) and Fig. 3 (f).

In order to find more correlations between transport and transmon-type measurements, we further compare the qubit punch-out, flux-tunability of cavity frequency and DC critical current of SQUID for three devices, as shown in Fig. 5. In the top panels of Fig. 5, the dispersive shift is 13.67 MHz, 0.48 MHz and 0.68 MHz for device 1, 2 and 3, respectively; while in the middle panels the maximal flux-tunability of cavity frequency is 1 MHz, 0.23 MHz and 0.5 MHz for device 1, 2 and 3, respectively. In section IV of SM, we have estimated the qubit-cavity coupling strength g based on the SQUID critical current in the sub-lobe of Fraunhofer pattern. The estimated $g/2\pi$ for device 2 and 3 are small as 41.76 MHz and 68.5 MHz, which can account for the relatively small flux-tunability. However, the estimated $g/2\pi$ for device 1 is relatively large (318.9 MHz) while the flux-tunability is still small, and if the qubit frequency intersect with cavity frequency, a large Rabi splitting is expected, which was not observed in the middle panel of Fig. 5 (a). We attribute this to the asymmetry of the SQUID in device 1 as compared to device 2 and device 3, as revealed in

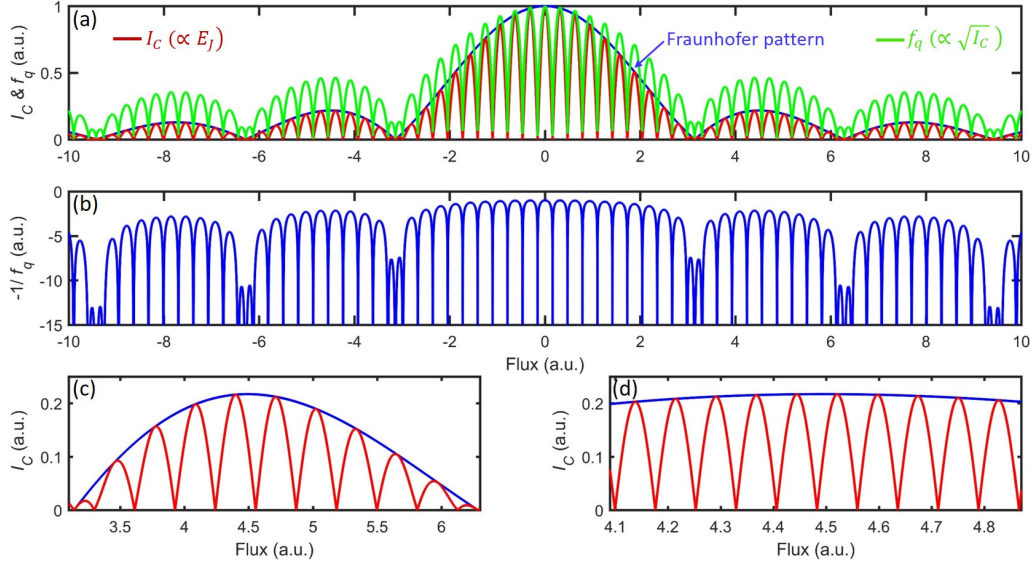


FIG. 4: Schematic simulation of SQUID critical current, qubit frequency and dispersive shift modulated by flux under the influence of Fraunhofer effect. More details can also be found in section III of SM. (a) SQUID critical current (I_C , red) and qubit frequency (f_q , green) modulated periodically by flux, with the blue curves indicating the Fraunhofer pattern. Note that we have set 10 oscillations in a sub-lobe (20 oscillations in the central lobe) to emulate the situation in Fig. 3(a). (b) Dispersive shift modulated periodically by flux. (c) Showing 10 oscillations in critical current when a Fraunhofer sub-lobe contains 10 SQUID oscillations. (d) Showing 10 oscillations in critical current when a Fraunhofer sub-lobe contains 40 SQUID oscillations. (c) and (d) are zoom-in images of Fig. S4(a) and (b) with a selected range.

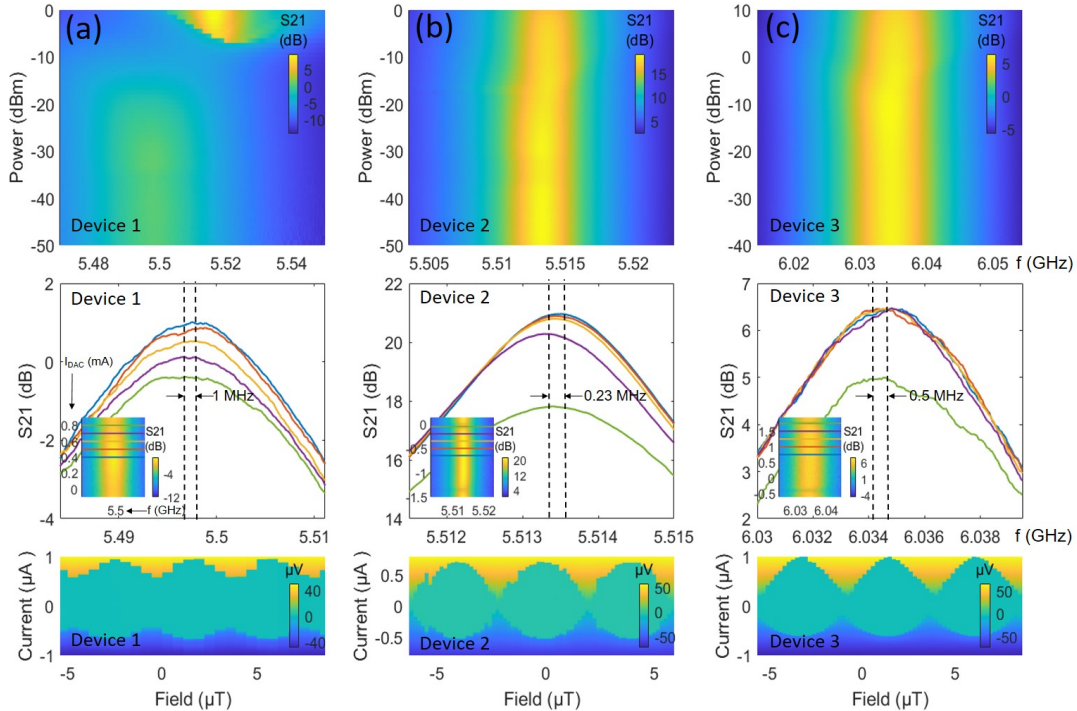


FIG. 5: (a) Top panel: Qubit punch-out measurements for device 1. Middle panel: Linecut along the frequency direction indicated by the colored lines in the inset. Inset: Flux modulation of cavity frequency across one period. Bottom panel: Oscillation of SQUID critical current for device 1 in a small B-field range. (b) The same as (a) but for device 2. (c) The same as (a) but for device 3.

the bottom panels of Fig. 5, which show three SQUID critical current oscillations for each device. The asym-

metry of the SQUID and the resulting skewed current phase relation (CPR) have been studied in graphene and InAs junctions before [33, 34]. It has been shown that the asymmetry in the SQUID inductance (α_L) and JJs (α_I) will both account for the distorting nonsinusoidal SQUID oscillations, while the minimum value of SQUID critical current $I_{C,min}$ only depends on the JJs asymmetry (α_I) [35]. With increasing α_I , $I_{C,min}$ increases, leading to a reduction of modulation depth of SQUID critical current $(I_{C,max} - I_{C,min})/I_0$, where I_0 is the average critical current of the two junctions [35]. This situation can be clearly observed in the bottom panels of Fig. 5, where $I_{C,min}$ around $0.6 \mu\text{A}$ for device 1 is higher compared to that for device 2 and 3 around $0.1 \mu\text{A}$ and $0.2 \mu\text{A}$, leading to a smaller modulation depth of SQUID critical current in device 1 as compared to device 2 and 3. This indicates a highly asymmetric SQUID in device 1 as compared to device 2 and 3 (also see relevant discussions in section V of SM). The transmons made of SQUID with asymmetric JJs have been investigated before in ref. [24]. The modulation of E_J with applied flux Φ in such a transmon is described by $E_J(\Phi) = E_{J\Sigma} \sqrt{\cos^2(\Phi) + d^2 \sin^2(\Phi)}$, where $E_{J\Sigma} = E_{J1} + E_{J2}$ and $d = (\gamma - 1)/(\gamma + 1)$ is the junction asymmetry parameter, with $\gamma = E_{J2}/E_{J1}$ (subscript 1 and 2 denote the JJ index) [24]. A large junction asymmetry parameter will result in qubit frequency oscillating at its maximal frequency with suppressed flux sensitivity (see section V in SM). As shown in Fig. S7 (a), the qubit frequency for device 1 oscillating between 12.935 GHz and 10.02 GHz is well above without intercepting with the cavity frequency around 5.5 GHz, leading to the small flux-tunability in cavity frequency even with a large qubit-cavity coupling strength g . In contrast, the SQUIDs are more symmetric in device 2 and 3, in which qubit frequency oscillation intersects with cavity frequency around 5.5 GHz and 6 GHz, as shown in Fig. S7 (b) and (c), respectively. We find supports to our simulations (Fig. S7) in our flux-modulated cavity frequency data as shown in Fig. 6. Fig. 6 (a) shows the flux modulation of cavity frequency for all three devices while Fig. 6 (b) shows the corresponding linecuts along the dashed lines in Fig. 6 (a). Since $f_{q,2}$ intersect with cavity frequency around the central position while $f_{q,3}$ intersect with cavity frequency in a lower position in modulation as shown in Fig. S7 (b) and (c), one can expect that the ratio between the flux regions where $f_q < f_r$ and $f_q > f_r$ is different in two devices. This can be clearly observed in Fig. 6 (b), where the ratio between the length of line A (denoting the region where $f_q < f_r$) and line B (denoting the region where $f_q > f_r$) is larger in device 2 as compared to that in device 3. In contrast, $f_{q,1}$ oscillates well above the cavity frequency as shown in Fig. S7 (a), we expect the up-and-down modulation of $f_{q,1}$ will reflect on that in cavity frequency similarly. This is also observed in the left panel of Fig. 6 (b), where the ratio between the length of line A and B is close to

unity.

The estimated g/π is 83.5 MHz for device 2 and 137 MHz for device 3, indicating that an exchange of energy between qubit and cavity would occur with a period of 11.97 ns in device 2 and 7.3 ns in device 3, respectively. The fact that the avoided crossing was not observed in flux-tuning data [Fig. 3 (b) and (c)] implies the qubit loses its coherence before a full round-trip exchange of energy can occur between the qubit and the cavity (see section IV of SM). The coherence time of the qubit should be roughly two or three times longer to see a well-formed avoided crossing. This implies an upper bound of coherence time 24 - 36 ns for device 2 and 14.6 - 22 ns for device 3, which is in a reasonable range within the coherence times reported from graphene 2D transmons [2]. In future endeavors, we anticipate by replacing Si/SiO₂ substrate with Si or sapphire substrates to reduce the dielectric loss, while adding magnetic shielding and infrared radiation filters, can further improve the decoherence time properties of the graphene-based quantum circuits in our systems [36–39].

IV. SUMMARY AND PROSPECT

In summary, we have demonstrated and characterized a series of flux tunable graphene-based superconducting quantum circuits based on 3D transmon architectures. We observed Fraunhofer pattern modulation in both cavity frequency (microwave measurements) and SQUID critical current oscillations (transport measurements) in one device, and found the correlation between the two can be associated with an asymmetric SQUID. We have provided a schematic to illustrate the flux-modulated supercurrent, qubit frequency and dispersive shift under the influence of Fraunhofer effect, which was used to connect with our microwave and transport data. We have relied on the DC critical current analysis to extract both the transmon-related parameters (E_J , f_q and g) and information of SQUID symmetry, which were later correlated with the flux-modulated transmon behavior in microwave measurements. Our device architectures enabling both DC and microwave probes can be extended to other quantum materials, where the unconventional ABSs play a role and result in topological phenomenon such as nontrivial 4π -period supercurrent and qubit frequency [22, 23]. For example, one can first probe the missing $n=1$ Shapiro step in DC transport to reveal the possible existence of non-trivial 4π -periodic ABSs [40–42]. The same device can then be placed in a 3D cavity to probe the 4π modulation of qubit frequency using time-domain spectroscopy, with the possibility to avoid quasi-particle poisoning. Our studies pave the way towards integrating novel materials for exploration of new types of quantum devices for future technology while probing underlying physics in the composite materials.

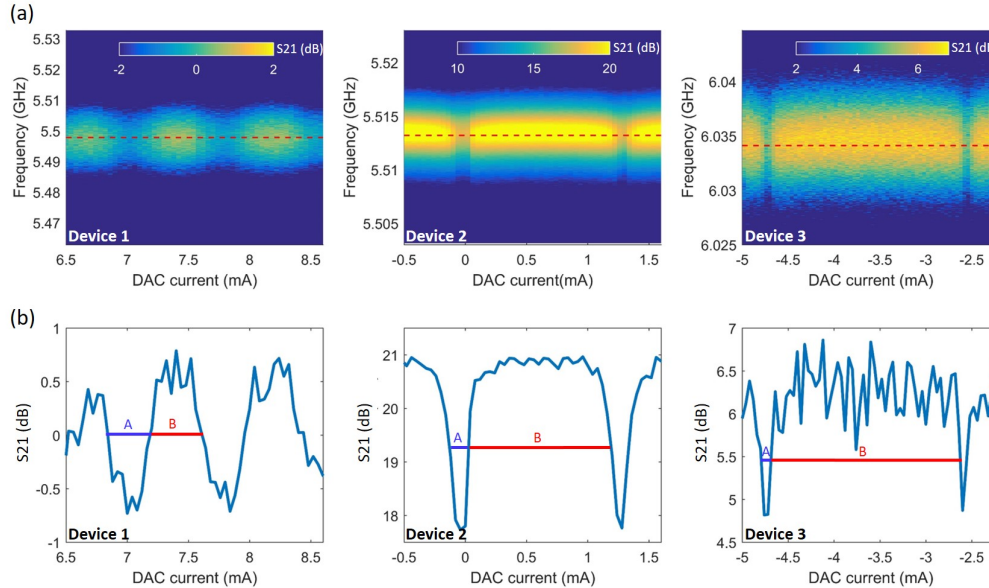


FIG. 6: (a) Flux modulation of cavity frequency for device 1, 2 and 3. (b) The corresponding linecuts along the red dashed lines in (a). For device 2 and 3, the lines labeled by A denote the flux range where $f_q < f_r$ while the lines labeled by B denote the flux range where $f_q > f_r$. For device 1, A and B denote the flux ranges for downward and upward behavior of the oscillating qubit frequency.

V. ACKNOWLEDGMENTS

Kuei-Lin Chiu would like to thank the funding support from National Science and Technology Council (Grant No. NSTC 109-2112-M-110-005-MY3 and NSTC 112-2112-M-110-017). Chung-Ting Ke and Yi-Chen Tsai would like to thank the funding support from National Science and Technology Council (Grant No. NSTC 110-2628-M-001-007). Kuei-Lin Chiu and Yen-Hsiang Lin also acknowledge support from the Center for Quantum Science and Technology (CQST) within the framework of the Higher Education Sprout Project by the Ministry of Education (MOE) in Taiwan.

Kuei-Lin Chiu would like to thank Valla Fatemi and Yueh-Nan Chen for the useful suggestions on the manuscript.

VI. AUTHOR CONTRIBUTIONS

K. L. Chiu conceived the project. Y. Chang fabricated the devices under the supervision of C. T. Ke. Y. H. Chen and A. J. Lasrado calibrated the 3D cavity with input from K. L. Chiu and Y. H. Lin. A. J. Lasrado performed the microwave measurements under the supervision of K. L. Chiu and with contributions from C. H. Lo, T. Y. Hsu and Y. C. Chen. Y. Chang performed the DC transport measurements under the supervision of C. T. Ke and with contributions from Y. C. Tsai. Samina and A. J. Lasrado performed the capacitance simulation

under the supervision of Y. H. Lin. K. L. Chiu and C. T. Ke co-supervise the project.

VII. COMPETING FINANCIAL INTERESTS

The authors declare no competing financial interests.

-
- [1] J. G. Kroll, W. Uilhoorn, K. L. van der Enden, D. de Jong, K. Watanabe, T. Taniguchi, S. Goswami, M. C. Cassidy, and L. P. Kouwenhoven, *Nature Communications* **9**, 4615 (2018), ISSN 2041-1723, URL <https://doi.org/10.1038/s41467-018-07124-x>.
 - [2] J. I.-J. Wang, D. Rodan-Legrain, L. Bretheau, D. L. Campbell, B. Kannan, D. Kim, M. Kjaergaard, P. Krantz, G. O. Samach, F. Yan, et al., *Nature Nanotechnology* **14**, 120 (2019), ISSN 1748-3395, URL <https://doi.org/10.1038/s41565-018-0329-2>.
 - [3] L. Casparis, M. R. Connolly, M. Kjaergaard, N. J. Pearson, A. Kringhøj, T. W. Larsen, F. Kuemmeth, T. Wang, C. Thomas, S. Gronin, et al., *Nature Nanotech* **13**, 915–919 (2018), URL <https://doi.org/10.1038/s41565-018-0207-y>.
 - [4] A. Hertel, M. Eichinger, L. O. Andersen, D. M. van Zanten, S. Kallatt, P. Scarlino, A. Kringhøj, J. M. Chavez-Garcia, G. C. Gardner, S. Gronin, et al., *Phys. Rev. Applied* **18**, 034042 (2022), URL <https://journals.aps.org/prapplied/abstract/10.1103/PhysRevApplied.18.034042>.
 - [5] C.-H. Lo, Y.-H. Chen, A. J. Lasrado, T. Kuo, Y.-Y. Chang, T.-Y. Hsu, Y.-C. Chen, G.-P. Guo, and K.-L.

- Chiu, SPIN p. 2340021 (2023), ISSN 2010-3247, URL <https://doi.org/10.1142/S2010324723400210>.
- [6] T. W. Larsen, K. D. Petersson, F. Kuemmeth, T. S. Jespersen, P. Krogstrup, J. Nygård, and C. M. Marcus, Phys. Rev. Lett. **115**, 127001 (2015), URL <https://link.aps.org/doi/10.1103/PhysRevLett.115.127001>.
- [7] G. de Lange, B. van Heck, A. Bruno, D. J. van Woerkom, A. Geresdi, S. R. Plissard, E. P. A. M. Bakkers, A. R. Akhmerov, and L. DiCarlo, PRL **115**, 127002 (2015), URL <https://link.aps.org/doi/10.1103/PhysRevLett.115.127002>.
- [8] J. Huo, Z. Xia, Z. Li, S. Zhang, Y. Wang, D. Pan, Q. Liu, Y. Liu, Z. Wang, Y. Gao, et al., Chinese Physics Letters **40**, 047302 (2023), ISSN 0256-307X, URL <https://dx.doi.org/10.1088/0256-307X/40/4/047302>.
- [9] K.-L. Chiu and Y. Xu, Physics Reports **669**, 1 (2017), ISSN 0370-1573, single-electron Transport in Graphene-like Nanostructures, URL <http://www.sciencedirect.com/science/article/pii/S0370157316303933>.
- [10] X. Liu and M. C. Hersam, Nature Reviews Materials **4**, 669 (2019), ISSN 2058-8437, URL <https://doi.org/10.1038/s41578-019-0136-x>.
- [11] K. L. Chiu, in *21st Century Nanoscience—A Handbook: Nanophotonics, Nanoelectronics, and Nanoplasmonics* (CRC Press, 2020), pp. 13–1–13–48.
- [12] I. Siddiqi, Nature Reviews Materials **6**, 875 (2021), ISSN 2058-8437, URL <https://doi.org/10.1038/s41578-021-00370-4>.
- [13] M. Hays, V. Fatemi, K. Serniak, D. Bouman, S. Diamond, G. de Lange, P. Krogstrup, J. Nygård, A. Geresdi, and M. H. Devoret, Nature Physics **16**, 1103 (2020), ISSN 1745-2481, URL <https://doi.org/10.1038/s41567-020-0952-3>.
- [14] M. Hays, V. Fatemi, D. Bouman, J. Cerrillo, S. Diamond, K. Serniak, T. Connolly, P. Krogstrup, J. Nygård, A. Levy Yeyati, et al., Science **373**, 430 (2021), URL <https://doi.org/10.1126/science.abf0345>.
- [15] A. Antony, M. V. Gustafsson, G. J. Ribeill, M. Ware, A. Rajendran, L. C. G. Govia, T. A. Ohki, T. Taniguchi, K. Watanabe, J. Hone, et al., Nano Lett. **21**, 10122 (2021), ISSN 1530-6984, URL <https://doi.org/10.1021/acs.nanolett.1c04160>.
- [16] J. I.-J. Wang, M. A. Yamoah, Q. Li, A. H. Karamlou, T. Dinh, B. Kannan, J. Braumüller, D. Kim, A. J. Melville, S. E. Muschinske, et al., Nature Materials **21**, 398 (2022), ISSN 1476-4660, URL <https://doi.org/10.1038/s41563-021-01187-w>.
- [17] K.-H. Lee, S. Chakram, S. E. Kim, F. Mujid, A. Ray, H. Gao, C. Park, Y. Zhong, D. A. Muller, D. I. Schuster, et al., Nano Lett. **19**, 8287 (2019), ISSN 1530-6984, URL <https://doi.org/10.1021/acs.nanolett.9b03886>.
- [18] L. Fu and C. L. Kane, Phys. Rev. B **79**, 161408 (2009), URL <https://link.aps.org/doi/10.1103/PhysRevB.79.161408>.
- [19] K.-L. Chiu, D. Qian, J. Qiu, W. Liu, D. Tan, V. Mosalanejad, S. Liu, Z. Zhang, Y. Zhao, and D. Yu, Nano Lett. **20**, 8469 (2020), ISSN 1530-6984, URL <https://doi.org/10.1021/acs.nanolett.0c02267>.
- [20] T. W. Schmitt, M. R. Connolly, M. Schleenvoigt, C. Liu, O. Kennedy, J. M. Chávez-García, A. R. Jalil, B. Benemann, S. Trellenkamp, F. Lentz, et al., Nano Lett. **22**, 2595 (2022), ISSN 1530-6984, URL <https://doi.org/10.1021/acs.nanolett.1c04055>.
- [21] X. Sun, B. Li, E. Zhuo, Z. Lyu, Z. Ji, J. Fan, X. Song, F. Qu, G. Liu, J. Shen, et al., Appl. Phys. Lett. **122**, 154001 (2023), ISSN 0003-6951, URL <https://doi.org/10.1063/5.0140079>.
- [22] D. M. Badiane, L. I. Glazman, M. Houzet, and J. S. Meyer, Comptes Rendus Physique **14**, 840 (2013), ISSN 1631-0705, URL <http://www.sciencedirect.com/science/article/pii/S1631070513001692>.
- [23] X. Sun, Z. Lyu, E. Zhuo, B. Li, Z. Ji, J. Fan, X. Song, F. Qu, G. Liu, J. Shen, et al., *Quasiparticle poisoning rate in a superconducting transmon qubit involving majorana zero modes* (2022), 2211.08094.
- [24] P. Krantz, M. Kjaergaard, F. Yan, T. P. Orlando, S. Gustavsson, and W. D. Oliver, Applied Physics Reviews **6**, 021318 (2020), URL <https://doi.org/10.1063/1.5089550>.
- [25] D. Rainis and D. Loss, PRB **85**, 174533 (2012), URL <https://link.aps.org/doi/10.1103/PhysRevB.85.174533>.
- [26] T. Karzig, W. S. Cole, and D. I. Pikulin, PRL **126**, 057702 (2021), URL <https://link.aps.org/doi/10.1103/PhysRevLett.126.057702>.
- [27] L. Wang, I. Meric, P. Y. Huang, Q. Gao, Y. Gao, H. Tran, T. Taniguchi, K. Watanabe, L. M. Campos, D. A. Muller, et al., Science **342**, 614 (2013), URL <http://www.sciencemag.org/content/342/6158/614.abstract>.
- [28] L. B. Nguyen, Ph.D. thesis (2020).
- [29] M. D. Reed, L. DiCarlo, B. R. Johnson, L. Sun, D. I. Schuster, L. Frunzio, and R. J. Schoelkopf, PRL **105**, 173601 (2010), URL <https://link.aps.org/doi/10.1103/PhysRevLett.105.173601>.
- [30] M. D. Reed, Ph.D. thesis, Yale University (2014).
- [31] J. M. Chow, Ph.D. thesis, Yale University (2010).
- [32] F. Qu, F. Yang, J. Shen, Y. Ding, J. Chen, Z. Ji, G. Liu, J. Fan, X. Jing, C. Yang, et al., Scientific Reports **2**, 339 (2012), ISSN 2045-2322, URL <https://doi.org/10.1038/srep00339>.
- [33] M. D. Thompson, M. Ben Shalom, A. K. Geim, A. J. Matthews, J. White, Z. Melhem, Y. A. Pashkin, R. P. Haley, and J. R. Prance, Appl. Phys. Lett. **110**, 162602 (2017), ISSN 0003-6951, URL <https://doi.org/10.1063/1.4981904>.
- [34] W. Mayer, M. C. Dartailh, J. Yuan, K. S. Wickramasinghe, E. Rossi, and J. Shabani, Nature Communications **11**, 212 (2020), ISSN 2041-1723, URL <https://doi.org/10.1038/s41467-019-14094-1>.
- [35] J. Clarke, *The SQUID handbook Vol 1 Fundamentals and technology of SQUIDS and SQUID systems* (Wiley VCH, Germany, 2004), URL http://inis.iaea.org/search/search.aspx?orig_q=RN:38047859.
- [36] W. D. Oliver and P. B. Welander, MRS Bulletin **38**, 816 (2013), ISSN 0883-7694, URL <https://www.cambridge.org/core/article/materials-in-superconducting-quantum-bits/B7A4DC8B7F54A0715CEFAFE6677F33D8>.
- [37] A. D. O'Connell, M. Ansmann, R. C. Bialczak, M. Hofheinz, N. Katz, E. Lucero, C. McKenney, M. Neeley, H. Wang, E. M. Weig, et al., Appl. Phys. Lett. **92**, 112903 (2008), ISSN 0003-6951, URL <https://doi.org/10.1063/1.2898887>.
- [38] A. D. Córcoles, J. M. Chow, J. M. Gambetta, C. Rigetti, J. R. Rozen, G. A. Keefe, M. Beth Rothwell, M. B. Ketchen, and M. Steffen, Appl. Phys. Lett. **99**, 181906 (2011), ISSN 0003-6951, URL <https://doi.org/10.1063/1.3658630>.

- [39] R. Barends, J. Wenner, M. Lenander, Y. Chen, R. C. Bialczak, J. Kelly, E. Lucero, P. O'Malley, M. Mariantoni, D. Sank, et al., *Appl. Phys. Lett.* **99**, 113507 (2011), ISSN 0003-6951, URL <https://doi.org/10.1063/1.3638063>.
- [40] J. Wiedenmann, E. Bocquillon, R. S. Deacon, S. Hartinger, O. Herrmann, T. M. Klapwijk, L. Maier, C. Ames, C. Brune, C. Gould, et al., *Nature Communications* **7**, 10303 (2016), URL <http://dx.doi.org/10.1038/ncomms10303>.
- [41] E. Bocquillon, R. S. Deacon, J. Wiedenmann, P. Leubner, T. M. Klapwijk, C. Brune, K. Ishibashi, H. Buhmann, and L. W. Molenkamp, *Nature Nanotechnology* **12**, 137 (2016), URL <http://dx.doi.org/10.1038/nnano.2016.159>.
- [42] C. Li, J. C. de Boer, B. de Ronde, S. V. Ramankutty, E. van Heumen, Y. Huang, A. de Visser, A. A. Golubov, M. S. Golden, and A. Brinkman, *Nature Materials* **17**, 875 (2018), ISSN 1476-4660, URL <https://doi.org/10.1038/s41563-018-0158-6>.
- [43] D. R., Y. F., MericI., LeeC., WangL., SorgenfreiS., WatanabeK., TaniguchiT., KimP., S. L., et al., *Nat Nano* **5**, 722 (2010), ISSN 1748-3387, URL <http://dx.doi.org/10.1038/nnano.2010.172>.
- [44] A. S. Mayorov, R. V. Gorbachev, S. V. Morozov, L. Britnell, R. Jalil, L. A. Ponomarenko, P. Blake, K. S. Novoselov, K. Watanabe, T. Taniguchi, et al., *Nano Lett.* **11**, 2396 (2011), ISSN 1530-6984, URL <http://dx.doi.org/10.1021/nl200758b>.
- [45] S. J. Haigh, A. Gholinia, R. Jalil, S. Romani, L. Britnell, D. C. Elias, K. S. Novoselov, L. A. Ponomarenko, A. K. Geim, and R. Gorbachev, *Nat Mater* **11**, 764 (2012), ISSN 1476-1122, URL <http://dx.doi.org/10.1038/nmat3386>.
- [46] I.-J. Wang, Doctoral dissertation, Harvard University (2016), URL <https://dash.harvard.edu/handle/1/26718763>.
- [47] A. Blais, R.-S. Huang, A. Wallraff, S. M. Girvin, and R. J. Schoelkopf, *PRA* **69**, 062320 (2004), URL <https://link.aps.org/doi/10.1103/PhysRevA.69.062320>.
- [48] G. Nanda, J. L. Aguilera-Servin, P. Rakyta, A. Kormanyos, R. Kleiner, D. Koelle, K. Watanabe, T. Taniguchi, L. M. K. Vandersypen, and S. Goswami, *Nano Lett.* **17**, 3396 (2017), ISSN 1530-6984, URL <https://doi.org/10.1021/acs.nanolett.7b00097>.
- [49] L. Maier, E. Bocquillon, M. Grimm, J. B. Oostinga, C. Ames, C. Gould, C. Brüne, H. Buhmann, and L. W. Molenkamp, *Physica Scripta* **2015**, 014002 (2015), ISSN 0031-8949, URL <https://dx.doi.org/10.1088/0031-8949/2015/T164/014002>.
-

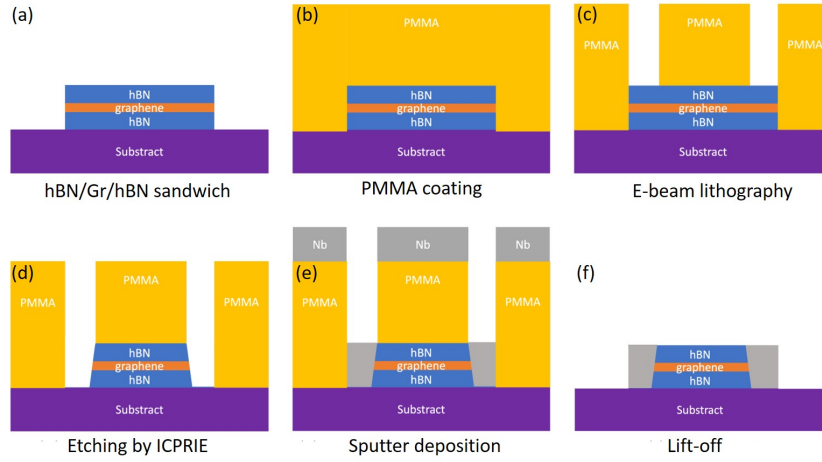


FIG. S1: Schematic diagrams of device fabrication process for our graphene-based superconducting quantum circuits. (a) hBN/Graphene/hBN sandwich after 2D material dry transfers. (b) Spin coating of PMMA. (c) E-beam lithography to define the patterns for SQUID contacts and capacitor pads. (d) Etching stack using ICP-RIE. (e) Deposition of Nb by sputter. (f) Lift-off to obtain graphene JJs with edge contacts.

Supplementary materials

I. DEVICE FABRICATION

The schematic diagrams for our device fabrication processes are illustrated in Fig. S1. We first prepare the hBN/graphene/hBN sandwich on intrinsic Si wafers capped with 90 nm SiO_2 (substrate) using the polymer-free dry transfer method [27, 43–45]. Fig. S2 (a) shows the optical micrograph of the as-transferred heterostructure (device 1), with a graphene flake encapsulated between two hBN layers. After spin coating of PMMA (A6, 500 rpm for 5 s then 4000 rpm for 55 s, bake at 170 °C for 2 mins), electron beam lithography (EBL) was used to define the pattern for capacitor pads and SQUID contacts. After EBL exposure and developing, the optical micrograph of device 1 at this stage is shown in Fig. S2 (b). In our SQUIDs, we have designed three contacts across the graphene layer, with a contact width of 2 μm and a 500 nm gap between each other. The extension of SQUID contacts connects to a pair of capacitor pads, each with a dimension of 600 μm \times 320 μm . In order to make edge contact to the encapsulated graphene, a Inductively Coupled Plasma Reactive-Ion Etching (ICP-RIE) technique was performed, using CHF_3 and O_2 gases with a ratio of 20:1 (power: 150 W and bias: 20 V), to selectively remove the hBN and graphene layers. This allows us to create the desired side contact geometry. Subsequently, 120 nm niobium (Nb) was sputtered (pressure: 3 mTorr, power: 25 W and sputtering rate: 6 nm/min) right after the etching process, ensuring minimal contact resistance. After lift-off, the optical micrograph of as-fabricated device 1 and device 3 are shown in Fig. S2 (c) and (d), respectively. Our 3D cavity transmon-type devices consist of two capacitor pads linking by two JJs. The capacitor pads not only form a shunting capacitor for transmon architecture but also work as an antenna to interact with microwave photons in 3D cavities.

II. MEASUREMENT SCHEME

Our 3D cavity transmon-type devices allow both microwave measurements and DC transport measurements. All the experiments detailed in the main text were performed in a dilution refrigerator with a base temperature of 10 mK. In this section, we will introduce the measurement scheme for both microwave [Fig. S3 (a)] and transport measurements [Fig. S3 (b)].

3D cavities need to be carefully calibrated before accommodating devices for microwave measurements. Our 3D copper cavity is milled from two pieces, one half consisting of a pin to drive qubits (drive port), and another with a pin to read qubits (readout port). The insertion depth of the pin within the ports determine pin's quality factors. Typically the readout port with lower quality factor consists of a longer pin, which has higher visibility to the cavity

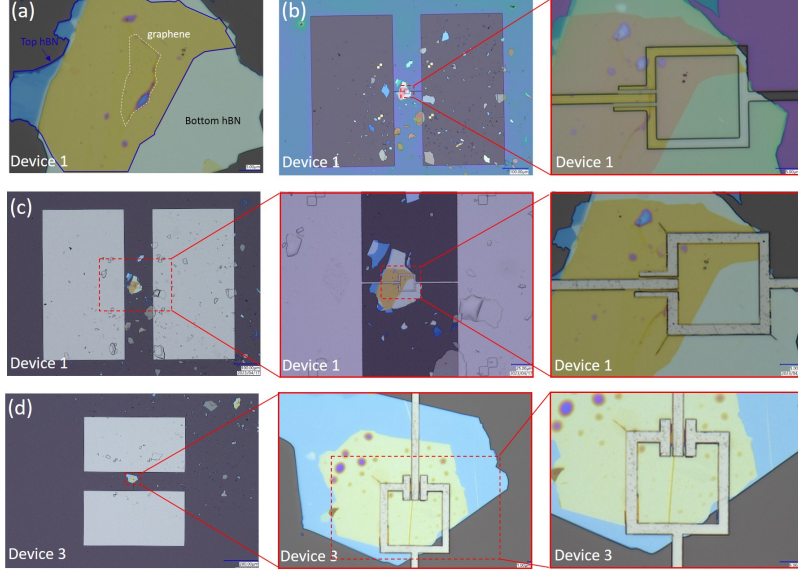


FIG. S2: Optical microscope images of device 1 at different stages in fabrication and the as-fabricated device 3. (a) Optical micrograph of hBN/Graphene/hBN sandwich structure after 2D material transfers. (b) Optical micrograph of device 1 after E-beam exposure and before ICP-RIE etching and Nb sputtering, with zoom-in image showing the SQUID structure. (c) Optical microscope images of the as-fabricated device 1 with different magnifications. (d) Optical microscope images of the as-fabricated device 3 with different magnifications.

photons, and thus couples strongly with the EM fields. In contrast, the drive port with higher quality factor consists of a shorter pin, thus limiting the leakage of photons through it. The quality factor of each pin is found by the formula of reflection parameter $S_{11}(f) = \frac{2i(f-f_0)-f_0/Q_{ext}+f_0/Q_{int}}{2i(f-f_0)+f_0/Q_{ext}+f_0/Q_{int}}$, where f_0 is the cavity resonance frequency, Q_{ext} is the Q value of the tested pin, and Q_{int} is the internal Q value of the 3D cavity [28]. We measure S_{11} of each pin with Vector Network Analyzer (VNA), and use the above formula to fit the amplitude and phase curve to the measured data to obtain Q_{int} and Q_{ext} of each pin. By carefully cutting pins and measuring the Q_{ext} , we generally reach a desired Q_{ext} ratio of drive pin to the readout pin of about 3:1 [28].

The measurement of microwave through the two-ports 3D copper cavity is performed with a transmission setup, in which two sets of coaxial lines are utilized: readout-in line serving as the input line while readout-out line as the output line, as shown in Fig. S3 (a). Readout-in line sends microwave from the output port of VNA (Keysight E5071C) to the drive port of 3D cavity. Subsequently, the transmitted signal from the readout port of 3D cavity travels through the readout-out line, finally reaching the input port of the VNA. By using a power splitter, readout-in line can also receive microwave signals from the RF source (Rohde Schwarz SGS100A) to drive the qubit for two-tone measurements. Since the entry of thermal photons from room temperature sources into the cryogenic environment can critically excite the qubits, the readout-in line is heavily attenuated with three 20 dB attenuators connected at different stages of dilution refrigerator. On the other hand, the readout-out line, which has no attenuation (0 dB), is connected to the High Electron Mobility Transistor (HEMT) amplifier at the 4K stage. The HEMT (LNF-LNC4 8C) has about 40 dB of gain and a noise temperature of 2K. To shield the device from thermal radiation from the HEMT amplifier, a set of three isolators are installed. The readout signal is further amplified by two room-temperature amplifiers (in total 40 dB gain) before going into the input of the VNA. In order to provide the necessary magnetic flux, a home-made superconducting coil is used, which is powered by an external DC source (digital-to-analog converter, DAC). The entire measurement setup is illustrated in Fig. S3 (a).

DC measurement is conducted within a dilution refrigerator operating at a base temperature of 10 mK, as illustrated in Fig. S3 (b). To facilitate precise four-wire measurements, the samples are affixed using four-wire connections, comprising a DC current source, two voltage probes, and a ground. The DC current source is established by combining a Keithley DAC voltage source with a range of ± 10 V and a room temperature 1 M Ω resistor. This setup allowed to generate a stable current in a range of ± 10 μ A. Two voltage probes are positioned on either side of the SQUID device, and the resulting voltage difference was then amplified by a room-temperature voltage amplifier, featuring a fixed gain of 100. Throughout the manuscript, it is important to note that the current range and amplification factor

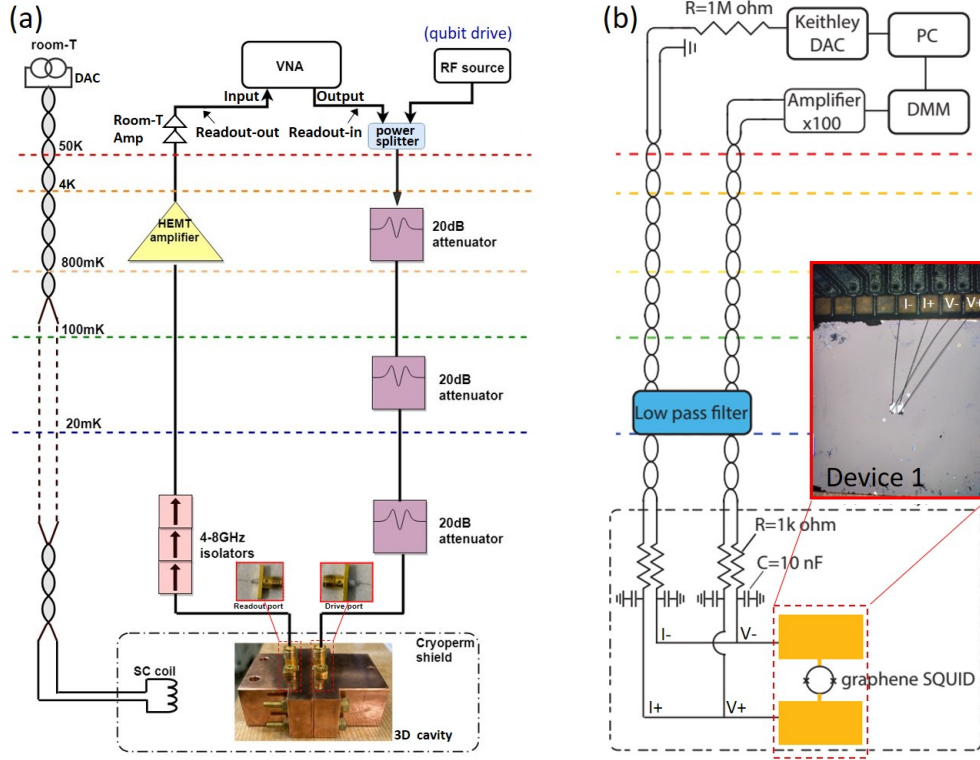


FIG. S3: (a) The measurement scheme used to perform the microwave characterizations, including qubit punch-out, flux modulation and two-tone spectroscopy of our graphene-based superconducting quantum circuits. (b) The measurement scheme used to perform the DC transport measurements of the same devices which were previously characterized by the microwave measurement scheme shown in (a).

remained consistent for all samples. To minimize the impact of external noise, twisted paired wiring is utilized from room temperature down to the mixing chamber level. To further enhance signal quality, two stages of low-pass RC filters are deployed at room temperature and on the printed circuit board (PCB). Additionally, a π filter from QDevil is incorporated at the mixing chamber level within the dilution refrigerator, serving the dual purpose of thermalization and noise reduction. All measurements and data acquisition are orchestrated through a dedicated PC.

III. SQUID OSCILLATIONS WITH FRAUNHOFER EFFECT

The supercurrent of a single junction considering Fraunhofer effect is described as $I_c(B) = I_c(0) \left| \sin\left(\frac{\pi B D' W}{\phi_0}\right) / \left(\frac{\pi B D' W}{\phi_0}\right) \right|$ [46]. Here, $I_c(0)$ is the critical current of junction at zero magnetic field, D is the junction length (parallel to supercurrent transmission direction), W is the junction width, ϕ_0 is the flux quanta, and $D' = D + 2\lambda_L$ is the effective junction length (λ_L is the London penetration depth). The SQUID oscillation modulated by JJ's Fraunhofer effect is described in equation 1 in the main text. In equation 1, the ratio between Φ_J and Φ , meaning the ratio between JJ's area ($D'W$) and SQUID loop area, determines the frequency ratio between the Fraunhofer oscillation and SQUID oscillation. In Fig. S4 (a) and (b), we plot the function $y = |\sin(x)/x| |\cos(A * x)|$, in which x represent the flux and the factor A (denoting the the area ratio between SQUID loop and JJ) sets to 10 and 40, respectively. This is to mimic the data as shown in Fig. 3 (a) and (d), in which 10 and 41 SQUID oscillations reside in a Fraunhofer sub-lobe, respectively. Note that in a real case, the period of SQUID oscillation is fixed (as the designed SQUID loop area for three devices are the same) while the period of JJ's Fraunhofer oscillation varies due to the variation of JJ's area (i.e., width of graphene flake) from device to device. Here, we fix the period of JJ's Fraunhofer oscillation while changing that of SQUID oscillation just for easy comparison of the ratio between two periods.

For an asymmetric SQUID with Fraunhofer pattern modulated by two different size junctions (the case of device

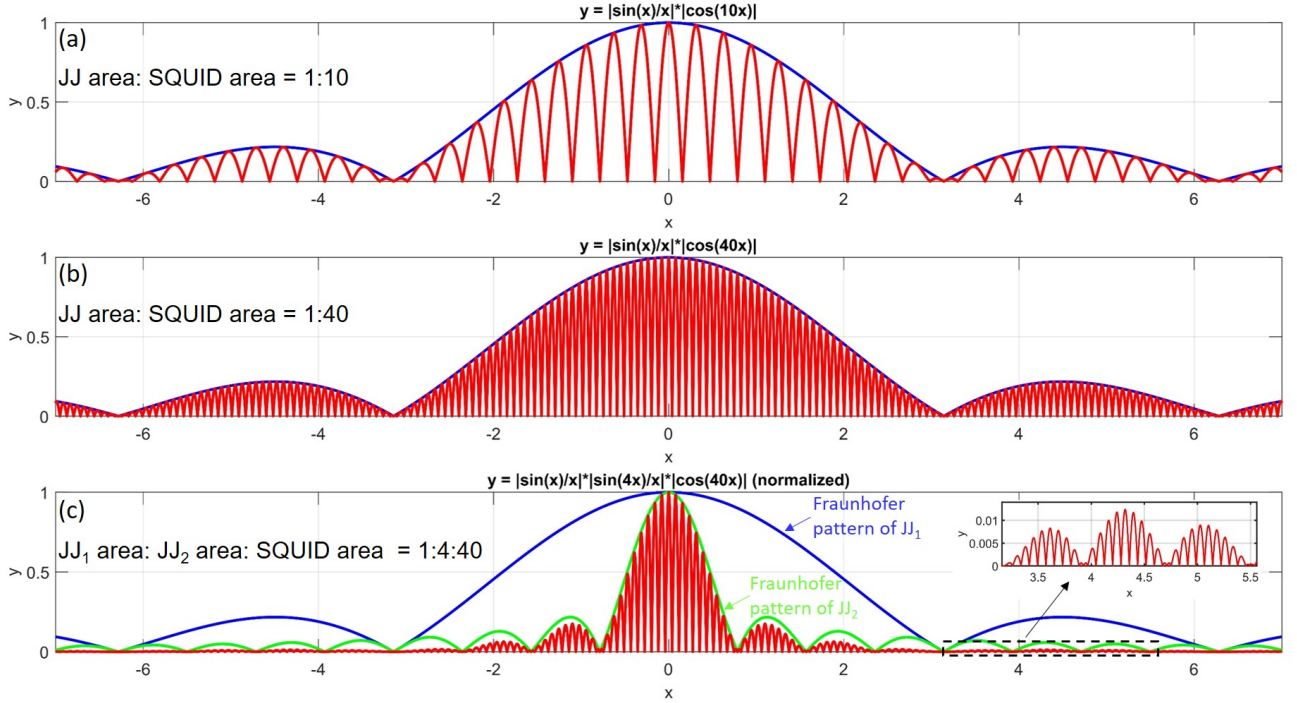


FIG. S4: (a) Schematic simulation of SQUID critical current (red curve) modulated by flux under the influence of Fraunhofer effect (blue curve), with 20 SQUID oscillations in the Fraunhofer central lobe. (b) The same as (a) but with 80 oscillations in the Fraunhofer central lobe. (c) Critical current (red curve) modulated by flux from an asymmetric SQUID, under the influence of Fraunhofer effect from two JJs with a area ratio 1:4. The blue curve denotes the Fraunhofer pattern of JJ_1 while the green curve denotes that of JJ_2 . All curves are normalized to 1. The inset shows the SQUID oscillations residing in three Fraunhofer sub-lobes of JJ_2 , which are located in the Fraunhofer sub-lobe of JJ_1 .

1), we construct the function as $y = |\sin(x)/x| |\sin(4x)/x| |\cos(40 * x)|$, in which the first term accounts for the Fraunhofer modulation from the smaller junction JJ_1 , the second term accounts for that from the larger junction JJ_2 , and the third term represents the SQUID oscillations. Note that here the function form of SQUID oscillation is still based on a symmetric SQUID, but it does not affect our analysis below as we mainly aim to discuss the interplay between two Fraunhofer patterns. The ratio between the factors 1:4:40 denotes the area ratio between JJ_1 , JJ_2 and SQUID loop, which is based on our analysis ($I_{C1} : I_{C2} = 1:4$ for device 1) in section V of SM. The function is plotted in Fig. S4 (c), with red curve indicating the total function value and blue (green) curve indicating the Fraunhofer pattern of JJ_1 (JJ_2). As can be seen, the SQUID oscillations modulated by a short-period Fraunhofer pattern from JJ_2 are further modulated by a long-period Fraunhofer pattern from JJ_1 . In our microwave measurements as shown in Fig. 3 (a), we observe the Fraunhofer modulation of JJ_2 whose sub-lobes contain 10 SQUID oscillations. However, we did not observe the full behavior as shown in Fig. S4 (c) in our transport data shown in Fig. 3 (d). We attribute this to the possible offset between the two Fraunhofer patterns induced by JJ_1 and JJ_2 . As an example, if JJ_2 's Fraunhofer central lobe is shifted to JJ_1 's Fraunhofer sub-lobe regions, meaning JJ_2 's Fraunhofer sub-lobes now locate in JJ_1 's Fraunhofer central lobe, one can imagine the SQUID oscillations residing in JJ_1 's Fraunhofer central lobe will not be much modulated by JJ_2 's sub-lobes, as the sub-lobe modulation is much weaker. We found relevant clues in the third cool down of device 1, in which we have performed the transport measurements again, as shown in Fig. S5. In Fig. S5 (a), the main features of Fraunhofer pattern remain almost the same as compared to Fig. 3 (d), with now 73 SQUID oscillations residing in the central lobe instead of 82 observed in the second cool down. However, this time we push the magnetic field range far away from the central lobe region, as shown in Fig. S5 (b). As can be seen, there is a new period of Fraunhofer lobe which contains only 22 SQUID oscillations, which is clearly not close to half of 73 and cannot be explained if considering a symmetric SQUID. Thus, this serves as an indication of the existence of another JJ with larger area compared to the one that induces 73 SQUID oscillations in the Fraunhofer central lobe.

In Fig. 4(b), we show the schematically simulated dispersive shift under the influence of Fraunhofer effect based on $\chi = -g^2/2\pi(f_q - f_r)$. We aim to understand how Fraunhofer pattern modify the periodically flux-modulated cavity frequency in SQUID-based transmons. To this purpose and for simplicity, we have set $g^2/2\pi = 1$ and $f_r = 0$

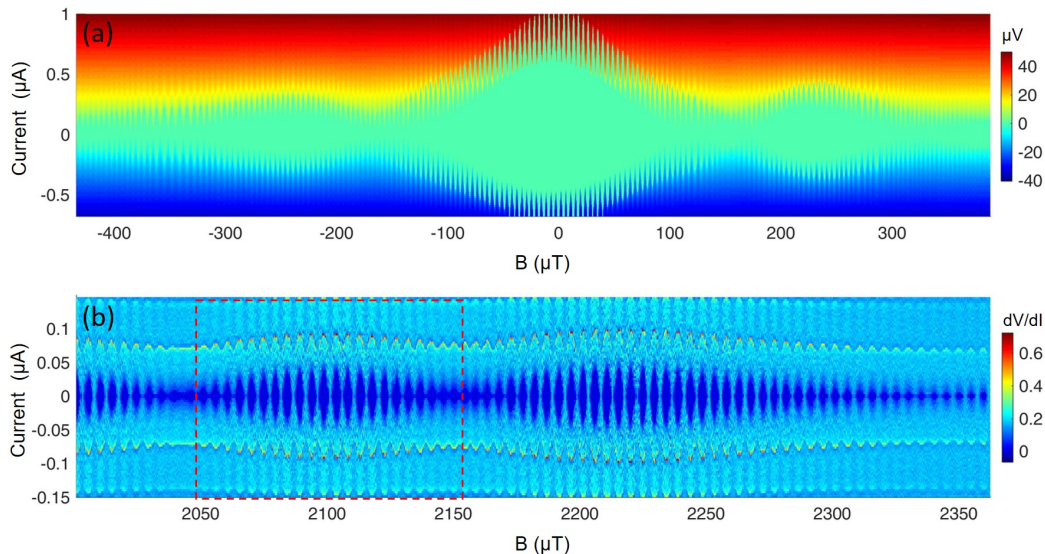


FIG. S5: (a) Flux modulation of SQUID critical current for device 1 in its third cool-down. (b) A Fraunhofer lobe (indicated by the red dashed square) which is far away from the central lobe and contains 22 SQUID oscillations. The raw data is differentiated along y-axis (current direction) in order to resolve the oscillations better.

as a reference point. We do this because the qubit punch-out measurements (top panels in Fig. 5) have indicated f_q at zero flux is higher than f_r in all devices. Also, in the flux region where $f_q \approx f_r$, a Rabi splitting will form and $\chi = -g^2/2\pi(f_q - f_r)$ is no longer valid. In Fig. S7, we have shown f_q oscillation with regard to cavity frequency for all devices. We are only interested in Fraunhofer modulation on the maximal f_q , which is well above f_r . Therefore, we set $f_r = 0$ as a reference and are only interested in the regime where $f_q > f_r$ in Fig. 4(b), by ignoring the function values at peculiar points where $f_q \approx 0$ that result in divergence in function values. We understand that the symmetry of SQUID for device 1-3 are different, which results in different critical current minimum hence determines whether f_q intersects with cavity frequency or not (see Fig. S7). However, since we are only interested in the Fraunhofer modulation on the maximal f_q , the results we got from Fig. 4(b) still hold regardless of SQUID symmetry.

The SQUID oscillation periods obtained from the bottom panels of Fig. 5 are $4.4 \mu\text{T}$ for device 1, $4.07 \mu\text{T}$ for device 2, and $4.728 \mu\text{T}$ for device 3, respectively. There exists a small deviation from the ideal period $\approx 8 \mu\text{T}$ estimated from the designed SQUID loop area ($16 \mu\text{m} \times 16 \mu\text{m}$), possibly due the fabrication error or different effective JJ areas in each device. We also note that the Fraunhofer patterns in the transport data exhibit small sample-dependent variations [Fig. 3(d), (e) and (f)], indicating the different uniformity of supercurrent in the junctions from device to device.

IV. COUPLING STRENGTH G ESTIMATION

By using Ansys Maxwell 3D software, we simulated the intrinsic capacitance between the capacitor pads along with non-connected SQUID contacts, including the effects of the cavity. By applying the voltage of 1V for one pad while keeping the other pad at 0 V, the capacitance between the pads is determined to be 92 fF. Based on the dispersive shift obtained from the qubit punch-out measurements, along with the SQUID critical current obtained from DC transport, we can estimate the qubit-cavity coupling strength g using $\Delta/2\pi = f_q - f_r$ and $\chi = g^2/\Delta$. Since qubit frequency $f_q \approx \sqrt{8E_J E_C}/h$, we need to know both charging energy $E_C = \frac{e^2}{2C}$ and Josephson energy $E_J = \frac{\Phi_0 I_C}{2\pi}$. We can first obtain $E_C/h \approx 210.5 \text{ MHz}$, using capacitance $C = 92 \text{ fF}$ obtained from our simulation. Next, we need to know SQUID critical current I_C to estimate E_J . Note that from our discussions in the main text, we speculate there exists a remanent magnetic field in our superconducting coil, so we have to choose the critical current residing in the Fraunhofer sub-lobe (i.e., outside central lobe region) in the transport data. Therefore, $I_C \approx 0.2 \mu\text{A}$ for device 1 [Fig. 3(d)], $I_C \approx 0.1 \mu\text{A}$ for device 2 [Fig. 3(e)] and $I_C \approx 0.2 \mu\text{A}$ for device 3 [Fig. 3(f)]. Hence, $E_J/h \approx 99.337 \text{ GHz}$ for device 1, $E_J/h \approx 49.668 \text{ GHz}$ for device 2 and $E_J/h \approx 99.337 \text{ GHz}$ for device 3. Combined all the parameters, we can estimate qubit frequency $f_q \approx 12.935 \text{ GHz}$ and $\Delta/2\pi = f_q - f_r = 12.935 \text{ GHz} - 5.4955 \text{ GHz} \approx 7.44 \text{ GHz}$ for

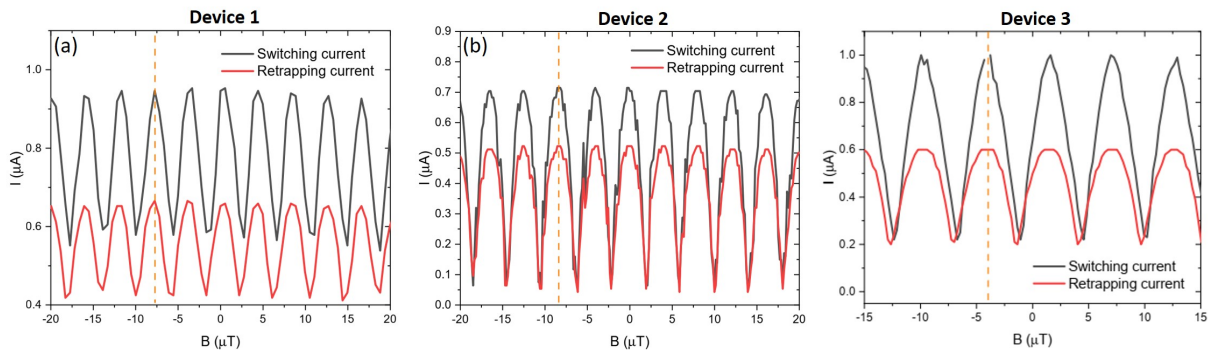


FIG. S6: The switching current and flipped retrapping current for (a) device 1, (b) device 2 and (c) device 3. The data is extracted from the data shown in Fig. 3 (d), (e) and (f).

device 1, $f_q \approx 9.146$ GHz and $\Delta/2\pi = f_q - f_r = 9.146$ GHz $- 5.5135$ GHz ≈ 3.63 GHz for device 2 and $f_q \approx 12.935$ GHz and $\Delta/2\pi = f_q - f_r = 12.935$ GHz $- 6.034$ GHz ≈ 6.9 GHz for device 3. Making $2\pi \times 13.67$ MHz $= \frac{g^2}{2\pi \times 7.44$ GHz}, $g/2\pi = 318.9$ MHz can be inferred for device 1; $2\pi \times 0.48$ MHz $= \frac{g^2}{2\pi \times 3.63$ GHz}, $g/2\pi = 41.76$ MHz can be inferred for device 2; $2\pi \times 0.68$ MHz $= \frac{g^2}{2\pi \times 6.9$ GHz}, $g/2\pi = 68.5$ MHz can be inferred for device 3. Note that all three devices have the same capacitor design and almost identical SQUID contact geometry. We attribute the variation of g in different devices to the different distribution of graphite flake remaining after the transfer process. We have tested the transmission (S_{21}) of the same cavity loaded with different devices (in similar designs) at room temperature, and found the total Q can vary from device to device. We suspect the remaining metallic graphite pieces interact with microwave, thus amend the distribution of electromagnetic field inside the cavity, thus causing the variation of the qubit-cavity coupling strength g in different devices.

In the next section, we found that the qubit frequency in device 2 and device 3 intersects with the cavity frequency [Fig. S7 (b) and (c)], while a Rabi splitting was not observed in the flux-tuning data as shown in Fig. 3(b) and (c). This indicates that device 2 and device 3 are not in the strong coupling regime: $g \gg \kappa$ and γ , where κ is the cavity decay rate and γ is the qubit total decay rate [47]. From the qubit punch-out measurements shown in the top panels of Fig. 5(b) and (c), we can estimate $\kappa/2\pi \approx 10$ MHz for device 2 and $\kappa/2\pi \approx 20$ MHz for device 3, based on the full width at half maximum (FWHM) of the cavity response at low powers. Thus, in both devices, $g/2\pi$ is large enough compared to $\kappa/2\pi$ (41.76 MHz > 10 MHz for device 2 and 68.5 MHz > 20 MHz for device 3), while Rabi splitting is still absent. This suggest that g is not greater than γ , from which we can estimate the upper bound of qubit coherence time as discussed in the main text.

V. SQUID SYMMETRY ANALYSIS

To give a qualitative analysis of the supercurrent in the individual Josephson junction of the SQUID, we plot the switching current and retrapping current as the function of the magnetic field as shown in Fig. S6 for device 1, 2 and 3. Based on the result of the current-to-phase (CPR) relationship in Fig. S6, we suggest that the inductance effect is small enough allowing us to analyze the supercurrent for each JJ. Firstly, the supercurrent shows a symmetric shape with respect to phase (magnetic field) without skewness for all devices (see bottom panels of Fig. 5). The asymmetry of CPR can come from the effect of the screening parameter β , which can be written as $\beta = I_{max} \cdot L/\phi_0$, where I_{max} is the maximum current through SQUID, L is the inductance, and ϕ_0 is the magnetic flux quanta. With a symmetric CPR (i.e, small β), this suggests that the influence of the inductance in the SQUID is negligible. Secondly, we compare the phase offset between switching and retrapping current, defined as $\Delta\phi = 2L(I_1 - I_2)$, where I_1 and I_2 are supercurrents for two Josephson junctions in SQUID. In Fig. S6, we plot the switching and retrapping current for all three devices by flipping the retrapping current to the positive side. From the orange dashed lines, we see almost no phase offset from switching respect with retrapping current in all devices. The small phase difference indicates that they are in either symmetric supercurrent case $I_1 = I_2$ or small loop inductance L case [48]. Clearly, for all devices, they are not in the case of $I_1 = I_2$ since the critical current does not reach zero (especially for device 1) as shown in the bottom panels of Fig. 5, from which we know L is close to zero. Thus, based on the two analyses, we conclude that the inductance is relatively small in our devices. With that, we are able to give a rough estimation of

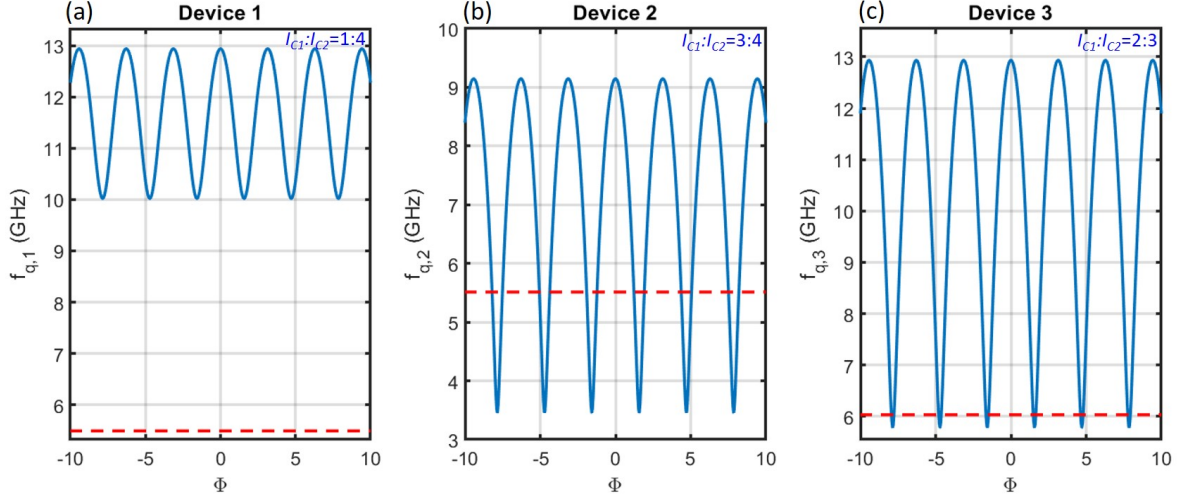


FIG. S7: Simulated qubit frequency modulation with respect to applied flux for (a) device 1, (b) device 2 and (c) device 3. The red dashed lines indicate the cavity frequencies.

the supercurrent for SQUID's JJs without complex calculation of the inductance of the SQUID system.

We follow ref. [49] to analyze the symmetry of SQUID in our devices. We chose the SQUID oscillations around $B = 0$ T as shown in the bottom panels of Fig. 5 for analysis. For two junctions with different critical currents $I_{C,i}$, $i = 1, 2$, the maximal SQUID critical current $I_{C,max}$ is $I_{C,1} + I_{C,2}$ while the minimal SQUID critical current $I_{C,min}$ is $I_{C,2} - I_{C,1}$. In device 1, $I_{C,max} \approx 1 \mu\text{A}$ while $I_{C,min} \approx 0.6 \mu\text{A}$, from which we obtain $I_{C,1} \approx 0.2 \mu\text{A}$ and $I_{C,2} \approx 0.8 \mu\text{A}$. Similarly, $I_{C,max} \approx 0.7 \mu\text{A}$ ($1 \mu\text{A}$) while $I_{C,min} \approx 0.1 \mu\text{A}$ ($0.2 \mu\text{A}$) for device 2 (3), from which we obtain $I_{C,1} \approx 0.3 \mu\text{A}$ ($0.4 \mu\text{A}$) and $I_{C,2} \approx 0.4 \mu\text{A}$ ($0.6 \mu\text{A}$) for device 2 (3). Thus, since $E_J \propto I_C$, $E_{J1}:E_{J2}$ is 1:4 for device 1, 3:4 for device 2 and 2:3 for device 3, respectively. Using $f_q \approx \sqrt{8E_J E_C}/h$ and $E_J(\Phi) = E_{J\Sigma} \sqrt{\cos^2(\Phi) + d^2 \sin^2(\Phi)}$ [24] as depicted in the main text, where $\gamma = 4$ ($4/3$ and $3/2$) and $d = 3/5$ ($1/7$ and $1/5$) for device 1 (2 and 3), we plot f_q as a function of Φ in Fig. S7. Note that we have combined all the parameters ($E_{J\Sigma} \sqrt{8E_C}/h$) to match $f_{q,max} = 12.935$ GHz, 9.146 GHz and 12.935 GHz for device 1, 2 and 3, as estimated in section IV in SM. We did this as we only care about how SQUID symmetry (the ratio between I_{C1} and I_{C2}) impact the oscillation depth of qubit frequency. As can be seen in Fig. S7, $f_{q,1}$ oscillate weakly between 12.935 GHz and 10.02 GHz without intersecting with cavity frequency at 5.4955 GHz, while $f_{q,2}$ and $f_{q,3}$ from more symmetric SQUIDs oscillate more strongly and intersect with cavity frequencies at 5.5135 GHz and 6.034 GHz, respectively.